Low energy electron transmission through layered materials and chiral organic films

Neu, P.S.

1 INTRODUCTION

1.1 Van der Waals materials

Graphene, a material consisting of carbon atoms arranged in a planar hexagonal lattice, exhibits many mechanical and electronic properties intrinsically linked to its two-dimensional (2D) nature. Although monolayer graphene is only one atom thick, it is surprisingly strong [1–3], making it ideal as a membrane for electron microscopy. The mechanical strength comes from the covalent bonds between the carbon atoms, that naturally all occur in a plane. Furthermore, the electronic properties resulting from the 2D honeycomb structure are remarkable: the band structure of graphene has a linear dispersion relation at the Fermi level, also called a photon-like dispersion [4]. In other words, the electrons have zero effective mass.

When going from one layer of graphene to two layers, i.e., bilayer graphene, even more interesting electronic properties may occur. In the natural stacking, where the second hexagonal lattice is shifted by half a diagonal of the hexagon (AB or Bernal stacking), the valence and conduction band avoid each other parabolically (zero bandgap semiconductor) [5]. However, when stacking two graphene layers with a twist angle of approximately 1.1°, called the magic angle, such 'twisted bilayer graphene' (TBG) was shown to be superconducting [6]. The associated flat bands [7] are a result of the larger moiré superlattice forming due to the twist and were predicted for certain, magic angles only [8].

The crucial step towards graphene research was to separate single graphene layers from the mother material graphite by the so-called 'scotch-tape exfoliation' method [9]. Graphite can be seen as a crystal in which many graphene layers are on top of each other, with a weak, van der Waals coupling between these layers. Therefore, layers of graphene can be pulled apart from the graphite by sticking scotch tape to the top and bottom. By iteratively applying this scotch-tape exfoliation method the first monolayer graphene samples were produced from graphite, a method that led to the Physics Nobel prize for Geim and Novoselov.

Graphene is not the only material that can be thinned down to single layers; there is an entire family. Such materials, that only have relatively weak van der Waals bonds between well-defined layers and covalent bonds within the layers, are known as the class of van der Waals (vdW) materials. Van der Waals materials come in different forms, varying from graphene, with a purely planar structure and only carbon atoms, to more complicated structures containing several atomic species per unit layer.

The electrical properties of vdW materials strongly depend on the number of layers. For example, a monolayer of molybdenum disulfide (MoS_2) is a direct band gap semiconductor, but a MoS_2 multilayer has an indirect band gap. Furthermore, the low defect density (per area) makes few-layer materials suitable as single photon emitters [10]. Imaging 2D materials with low energy electrons will allow us to identify sample areas of different composition and band structure, that typically form in the growth and fabrication process.

The systems studied in this thesis are sketched in Figure 1.1. They reach from the conducting graphene (a), via the insulating hexagonal boron nitride (hBN, b) consisting of two elements in the same plane, to semiconducting molybdenum disulfide (MoS_2, c), a so-called transition metal dichalcogenide, or TMD. The materials in Figure 1.1 all share a 2D honeycomb structure. Out of plane, these layers can be arranged differently, with the preferred atomic orientation shown

in the bottom row. MoS_2 is different from graphene and hBN, as the atoms in a unit layer are still arranged in different atomic sheets, with the Mo plane sandwiched between the S plane. This also allows for more variations in vertical stacking, known as polytypes, with the 2H polytype (Mo atoms and S atoms alternating in-plane positions each layer) being the most stable.

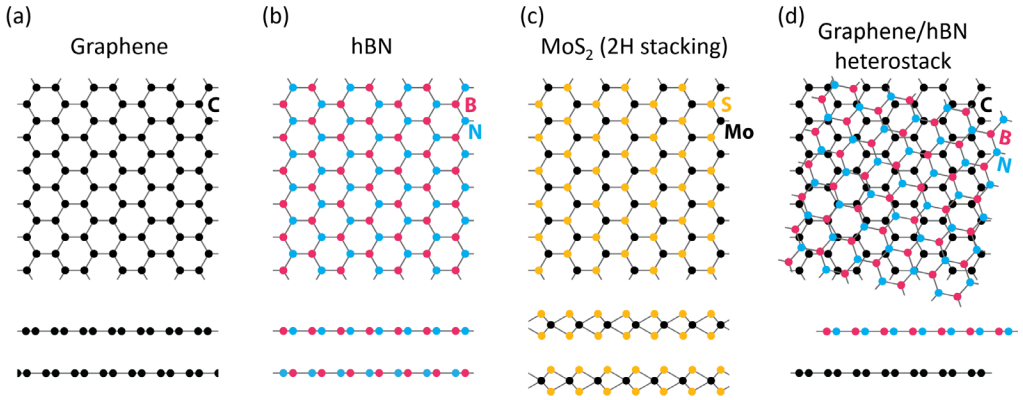

Figure 1.1: Atomic lattices of the two-dimensional materials studied in this thesis: graphene (a), hexagonal boron nitride (hBN, b), molybdenum disulfide (MoS_2, c) and a heterostack (d) of hexagonal boron nitride on top of graphene. The top row shows the in-plane structure. Note that only one layer is shown for the crystals a-c, whereas one layer of graphene and one layer of hBN is shown for the heterostack (d). The bottom row shows a side view of two layers. For the graphene, hBN and MoS_2 the preferred stacking order is shown.

By stacking layers of van der Waals materials, one can create materials that do not occur in nature. The resulting stack will thus have (electronic) material properties that differ from the original material(s). This is to some extent comparable to a reaction in chemistry, but easily reversible as the layers could be peeled apart again, the interaction between layers being relatively weak. After seeing the diversity of phenomena enabled by stacking two graphene layers, we can only imagine the rich possibilities of combining different van der Waals materials layer by layer.

In Figure 1.1d, a heterostack of hBN on graphene breaking the top-down symmetry of the system is shown. The graphene-hBN heterostack is common in experiments, as a hBN substrate is used for its insulating and flatness properties in device fabrication. Typically, the twist angle, randomly chosen in Fig. 1.1d, is not controlled. Part of the emergent electronic band structure of such a heterostack is investigated in Chapter 4.

1.2 Probing van der Waals materials with electrons

In this thesis, we will probe van der Waals materials using low energy electrons that have an energy range of about 0-50 eV. The basic experiment is shown in Figure 1.2: Electrons with a tunable energy E (above the vacuum energy) are directed towards the sample, e.g., a freestanding bilayer of MoS_2 as depicted in Figure 1.2. The electrons hit the sample at perpendicular incidence to the surface. Then the electron waves are either transmitted or reflected with a certain probability strongly depending on the electron energy. We note that the

point where the electrons are reflected is not well defined (like the arrow in Fig. 1.2 may suggest), as the scattering process is quantum mechanical. In practice, some electrons will also be scattered inelastically and/or absorbed by the material.

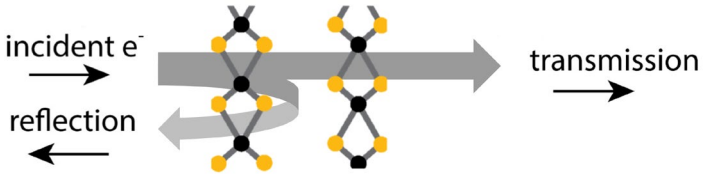

Figure 1.2: The basic idea of a reflection/transmission experiment with low-energy electrons. Electrons traveling in a vacuum are directed towards a few-layered sample. The electrons hit the sample (at perpendicular incidence to the 2D planes). The electron flux is partially reflected and partially transmitted.

In terms of experimental techniques, imaging the reflected electrons is known as low energy electron microscopy (LEEM) and imaging the transmitted electrons is named electron Volt-transmission electron microscopy (eV-TEM) [11]. Imaging refers to acquiring a spatially resolved image of the sample, rather than recording one reflectivity or transmissivity value. Recording a well-resolved 2D image of the sample is important, as samples typically consist of areas of different thickness and composition, resulting in different reflectivity/transmissivity. The microscopy techniques used will be described in more detail in Chapter 2.

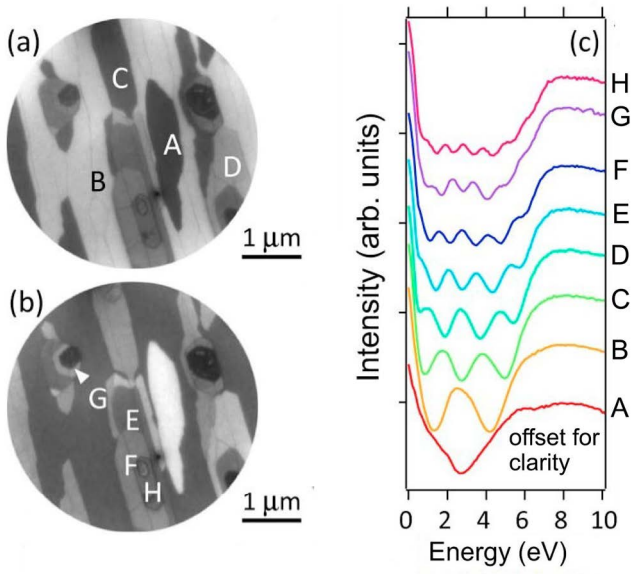

Figure 1.3: LEEM images of multilayer graphene grown on 4H-SiC recorded at 2.5 eV (a) and 4.5 eV (b) electron energy. Different brightness indicates different layer counts of graphene. The reflection spectra (c) recorded at the areas indicated in the image allow for determining the number of graphene layers by counting the number of minima between 0 to 6 eV (not counting the buffer layer). Reprinted from H. Hibino et al. [12].

As an example, two LEEM images (recorded at different electron energies by Hibino et al. [12]) of multilayer graphene grown on 4H silicon carbide (4H-SiC) are shown in Figure 1.3a/b. We see different areas of different brightness, where brighter means a higher electron reflectivity

at that energy. The LEEM reflection spectra, i.e., the reflectivity as a function of energy, of areas A-H are shown in Figure 1.3c. The spectrum of area A has one minimum in the 0-6 eV energy range. It has been shown [13,14] that this single minimum is characteristic of one layer of graphene on top of a graphene-like buffer layer (an electrically insulating layer that is partially bound to the underlying SiC). For each additional graphene layer, the minimum splits, such that the graphene layer number (not including the buffer layer) can be counted by counting the low-energy reflection minima. Above five minima (area E) it becomes unclear how to count the minima, as the lowest oscillations move below the vacuum level (zero energy) and oscillations above 6 eV move to the flank of the next feature in the spectrum. Still, the central minimum in area E becomes a maximum in F and again a minimum in G, and so on. We will model the reflection and transmission spectra of freestanding graphene with a model inspired by optical interference in Chapter 3.

1.3 Electron-Matter interactions

For electrons interacting with matter, the quantum-mechanical wave nature of the electron must be considered, with the de Broglie wavelength of the electron $\lambda = h/\sqrt{2m_\mathrm{e}E}$ (with the electron mass m_e). For a rule of thumb estimate, this reduces to $\lambda\,[\text{Å}] \approx \sqrt{150/E[\text{eV}]}$. Thus, the wavelength of few-eV electrons is comparable to lattice constants in crystals/van der Waals materials, which are typically in the order of Angstroms. The basic, elastic interaction of electrons with a van der Waals material can be understood from the quantum well model, known from quantum mechanics textbooks, as explored next [15,16].

1.3.1 Elastic electron scattering: the electron wave

The textbook example is the one-dimensional potential V shown in Figure 1.4a that takes a constant negative value V_0 in a finite well from 0 to d (in the material with thickness d) and is 0 otherwise (corresponding to the vacuum energy). To solve the scattering problem, i.e. find the amplitude of the reflected and transmitted electron wave at an energy E, we solve the stationary Schrödinger equation for the one-dimensional case

$$\left(-\frac{\hbar^2}{2m}\frac{d^2}{dx^2} + V(x)\right)\Psi(x) = E\,\Psi(x) \qquad (1)$$

where $\Psi(x)$ is the wave function and m is the electron mass.

For electrons with an energy above the vacuum level the Schrödinger equation of the quantum-well problem always has a solution (in fact two: the right-moving and left-moving electrons), called the unbound states[1].

We solve the (stationary) Schrödinger equation with an ansatz where the incident electron wave is normalized to one, i.e., $\Psi_{\rightarrow,\mathrm{vac}} = \exp(ikx)$, and there are no incoming electrons from the

[1] One can show that the reflection and transmission probability is the same for electrons incident from the left as for electrons incident from the right [16].

right vacuum side (see Fig. 1.2). This will result in outgoing waves from both sides of the well, one representing reflection and one representing transmission. The resulting electron densities $|\Psi^2|$, which include possible interferences, at four chosen energies are shown in panel (b), with the energies indicated in the reflection spectrum in (c).

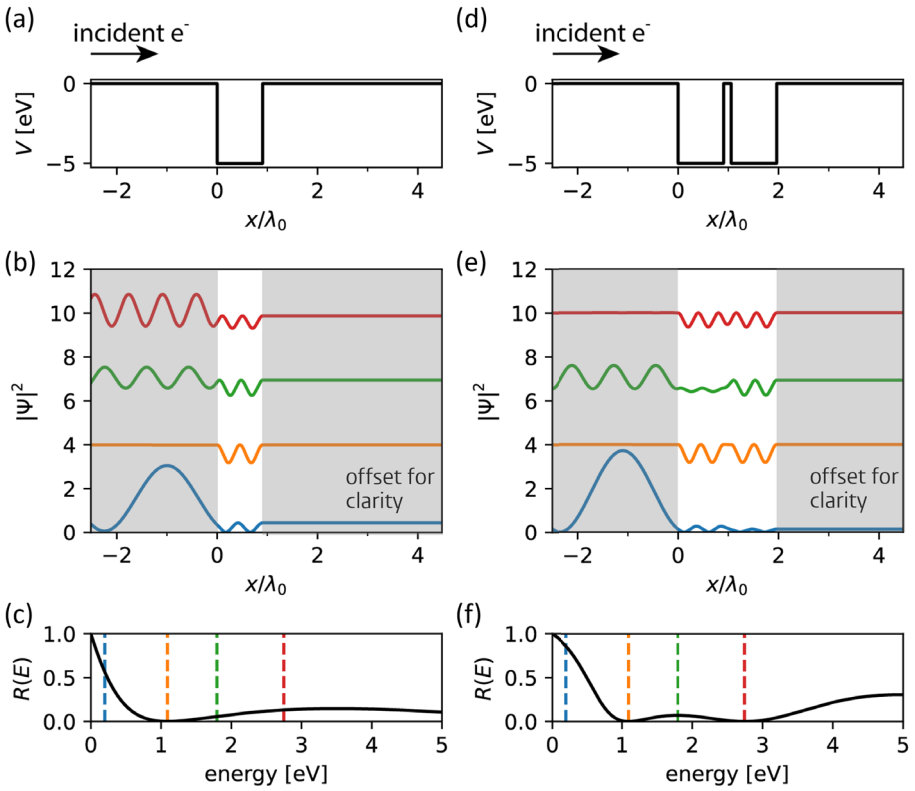

Figure 1.4: Quantum mechanical calculation of scattering of electrons from a finite quantum well (a) and a finite double well (d) with depth $V_0 = -5$ eV. The electrons are incident from the vacuum ($V = 0$) with an energy E above the vacuum level, like in a LEEM experiment. Panels b/e show the electron probability density for the respective cases at selected energies (marked in panels c/e). The calculated reflection spectra show one minimum for the single well and a second minimum forming for the double well in the plotted low-energy range. The spatial axis in (a, b, d, e) is given in units of the $\lambda_0 = h/\sqrt{2m_e(0 - V_0)}$, corresponding to the wavelength inside the well at $E = 0$ incident energy. The probability density curves (b,e) are offset for clarity by 0, 3, 6, and 9, and the incoming electron wave amplitude is normalized to $\hat{\Psi} = 1$.

To the left of the sample, the incident and reflected wave interfere and produce oscillations in $|\Psi|^2$. The yellow curve in (b) does not show the oscillations on the vacuum side, as the reflection amplitude is zero at that energy. As we are not considering absorption, the full electron flux is transmitted at that energy. We will call the unbound states with enhanced transmission the transmission states, or states for short.

Figure 1.4d shows a double potential well, i.e., two wells like in (a) separated by a thin barrier. In addition to the reflection minimum of the single well (marked in yellow), a new minimum (marked in red) around 2.7 eV forms in the reflection spectrum (see Fig. 1.4f). In both minima the reflected intensity is zero, thus there is no interference of the wavefunctions in the vacuum

(Fig. 1.4e). While the 1.1 eV state (yellow) has a maximum of probability density at the barrier, the 2.7 eV state (red) has a minimum there. We used the quantum well example to introduce 'transmission states' and show how adding a layer can affect the reflection (and transmission) spectrum. For a generalization to multiple wells using the scattering matrix method we refer to [17]. Arranging the wells into a periodic lattice and solving the Schrödinger equation will yield a band structure (c.f. [16,18]). As long as we only consider a few layers of 2D materials, thus only a discrete set of wavevectors fitting the layer spacing, the transmission states are discrete points in the out-of-plane band structure.

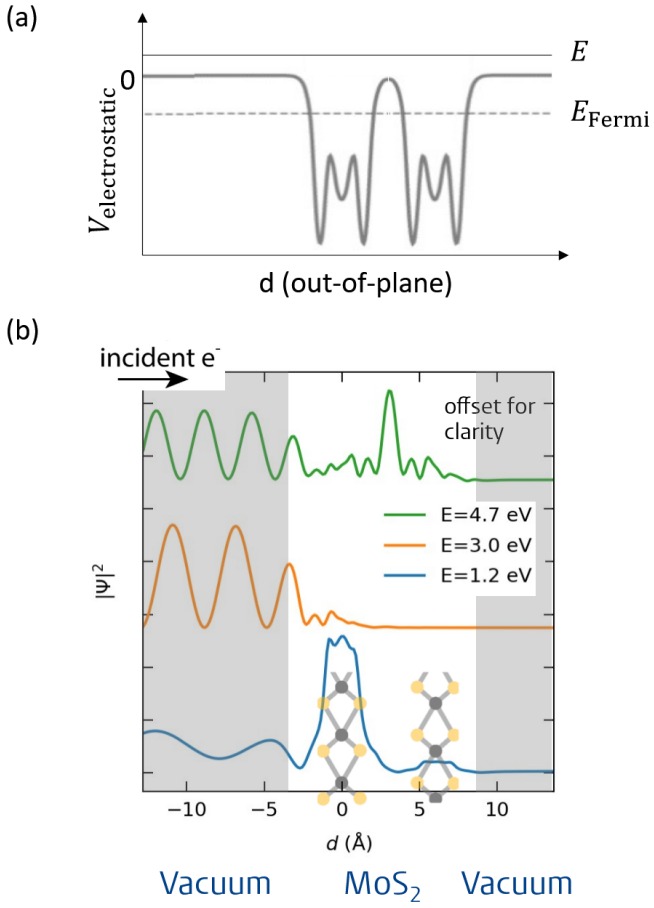

Figure 1.5: (a) Sketch of the electrostatic potential of bilayer MoS_2 projected onto the out-of-plane axis. The incident electron energy E is above the vacuum level (0) and the Fermi level (E_{Fermi}). The electron density (b) is shown at 3 electron energies, illustrating a state centered in the layer (1.2 eV) and a state (4.7 eV), centered between the layers ('interlayer state'). For an energy of 3.0 eV, there is no state available, and the signal is strongly attenuated within the material, leading to a relatively high reflectivity. The electron wave functions in MoS_2 were calculated in three dimensions (by E.E. Krasovskii, see Chapter 5) and then projected onto the out-of-plane axis. Panel a adapted from [19].

In reality, the potential well has to be replaced by the three-dimensional electrostatic potential in the material of interest to calculate the transmission and reflection probability of electrons. The electrostatic potential for bilayer MoS_2 and the solved electron density at three select energies are shown in Figure 1.5a and b, respectively. Both plots show the dependence on the out-of-plane dimension and are averaged along the two in-plane dimensions. All electron densities show characteristic oscillations on the left, as the electron wave incident from the left

interferes with its reflection. As all scattering is treated as elastic, the reflected and transmitted flux sum to the incident flux.

Remarkably, the electron density (Fig. 1.5b) at $E = 1.2$ eV is centered in the MoS_2 layers, whereas the electron density at $E = 4.7$ eV is centered in between the two layers. The states at $E = 1.2$ eV and $E = 4.7$ eV have a relatively high transmitted flux, while the electron density at $E = 3.0$ eV is shown as an example of maximal reflection (thus minimal transmission). In terms of band structure (above the vacuum level), the high transmission states correspond to the existence of a (dispersive) band in the travel direction of the electrons (out-of-plane direction, $\overline{A\Gamma}$ direction). We note that the band structure below the vacuum level, in particular at the Fermi level, cannot be imaged with electrons coming from and going to vacuum.

1.3.2 Elastic and Inelastic Mean Free Path

In addition to elastic scattering, the electrons will also undergo inelastic scattering processes, e.g., with phonons and plasmons. This will be discernible in our experiments, as we will filter in electron energy and angle. Electrons that lose energy to a value below the vacuum level are even absorbed in the material. In a macroscopic view, the characteristic length that an electron travels before being scattered is given by the energy-dependent mean free path (MFP) λ. Thus, the electron transmission probability through material of thickness d is generally given by $p_T(E) = \exp(-d/\lambda(E))$. Both inelastic and elastic scattering processes, with their respective mean free path lengths $\lambda_{inel.}$ and $\lambda_{el.}$, contribute to the MFP with $\lambda^{-1} = {\lambda_{inel.}}^{-1} + {\lambda_{el.}}^{-1}$.

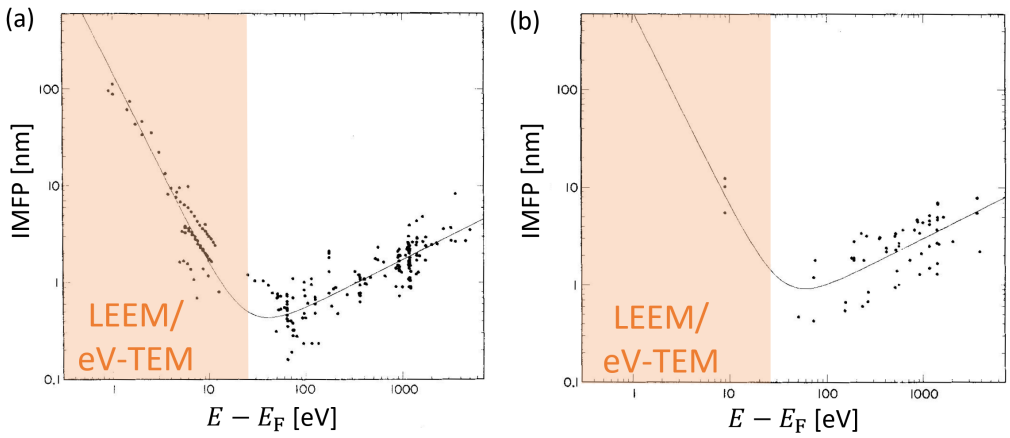

Figure 1.6: Inelastic electron mean free paths of elements (a) and inorganic compounds (b) compiled by Seah and Dench [20]. The data fit a general U-shape, called the 'universal curve', with a minimum at 30-40 eV (above the Fermi level). However, few data points are present (especially for inorganic compounds) in the low energy range where LEEM and eV-TEM operate. Data and fits from [20].

Although the MFP is a material property, the compilation of MFPs of different materials by Seah and Dench (reprinted in Fig. 1.5) shows that $\lambda_{inel.}(E)$ follow the same curve remarkably well for different materials. This curve, generally called the 'universal curve', was fitted to the datapoints of elements (Fig. 1.5a) and inorganic compounds (Fig. 1.5b). The curve describes a U-shape with a minimum at about 30-40 eV above the Fermi level. Conventional transmission electron microscopes (TEM) operate at high energies (100-1000 keV), where the mean free

path is large, and the electrons can penetrate micron-scale samples. Intuitively, the electron MFP increases for higher energies, as the faster electrons have less time to interact with the sample [21].

The MFP also increases towards very low energies because some energy losses, e.g., due to plasmons, require a minimal energy transfer. The lower the electron energy, the fewer of these losses can be excited and the larger the MFP becomes again. This has allowed our group to introduce transmission electron microscopy at low energies – eV-TEM [11,22–24]. The energies discussed in low energy electron microscopy are typically around or below the 'universal curve' minimum.

The MFP gives an estimate of the probing depth of reflected low-energy electrons and the intensity of transmitted electrons. Vice versa, measuring the transmitted and reflected electron spectra will allow us to determine the inelastic and elastic mean free paths. We will fill in the inelastic MFP curves for the abovementioned 2D materials (Fig. 1.1), as the low-energy side of the MFP curve for inorganic compounds (Fig. 1.5b, not elements) rests on only a few data points.

Strictly speaking, the universal curve only applies to isotropic materials, although one can still expect the MFP to increase towards the lowest energies, as fewer loss mechanisms become excitable. We will treat two-dimensional materials at perpendicular incidence, which are clearly anisotropic. Based on the elastic scattering calculations above, we should expect to see oscillations in the (total) MFP in cases with little inelastic scattering. We will use LEEM and eV-TEM in combination to determine the MFP in much more detail than before, compare to photoemission experiments and test the universality of the 'universal curve' in Chapters 3-5.

1.4 Chirality

An object is chiral when it lacks mirror symmetry, i.e., it cannot be superimposed onto its mirror image by translation and rotation. The eponymous example is the hand (from Greek kheir, χειρ = hand): While our hands are mirror images of each other, they cannot be moved or rotated in a way such that they are exactly equal. We note that chirality is defined in the context of spatial dimensionality. If we draw the outline of a left hand and a right hand on a piece of paper, they cannot be overlaid in two dimensions. However, if we cut out the outline of the hands, we can use the third dimension to flip one hand upside down and overlay them.

A specific case of chirality are helical structures, like the helical staircases on either side of our office in Leiden shown in Figure 1.7a. Other examples of helices in our everyday life are screws, springs, fusilli pasta, and the double helix of DNA. When looking along the axis of a helix (down the staircase in Fig. 1.7a), moving forward can either describe a clockwise rotation or an anti-clockwise rotation. If it is a clockwise motion, we call the helix right-handed (like a regular screw), and left-handed otherwise. Flipping a helix upside down does not change its handedness, as the handedness is an inherent property and a special case of chirality.

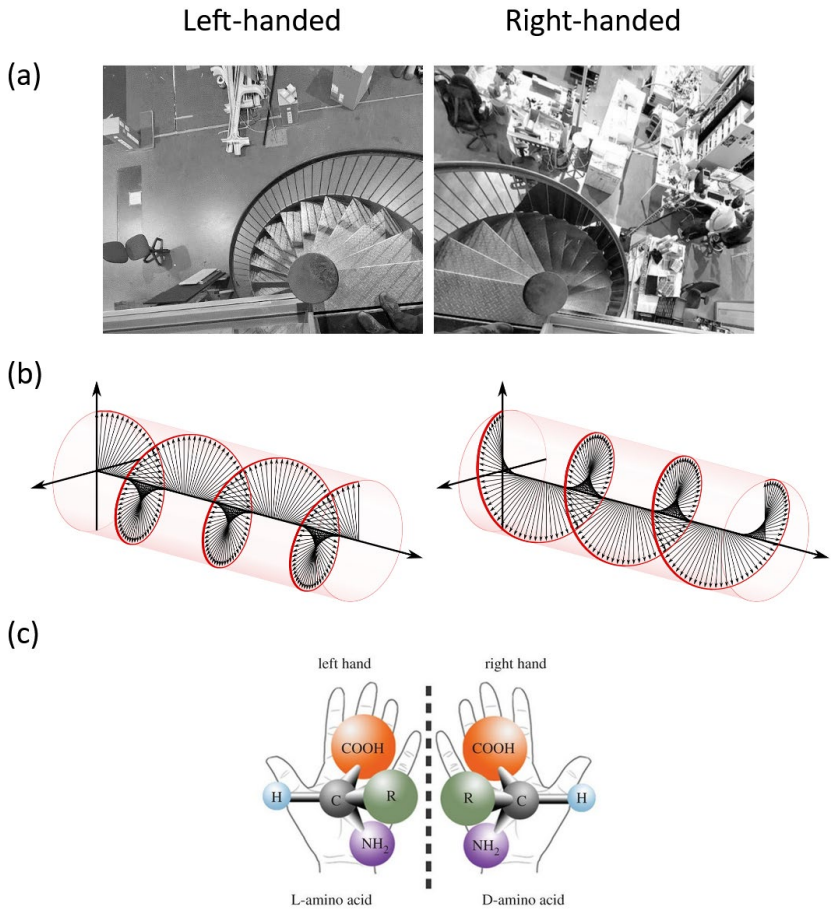

Figure 1.7: Examples of chirality, with the left-handed version on the left and the right-handed version on the right. The staircases (a) on either side of our office (Kamerlingh Onnes Laboratorium, Leiden University) are helical, with opposite handedness. For circularly polarized light (b), the electric field vector (of a wave frozen in time, optics textbook convention) describes a helix around the propagation direction. Molecules (c) that are chiral (but not necessarily helical) are named after their effect on light polarization: left-turning (levorotary, L) or right-turning (dextrorotary, D). The illustration (b) is licensed under the wikipedia creative commons license and reprinted from [25]. We acknowledge Inaki et al. [26] for publishing the figure in (c) in an open access article.

Also, the electric and magnetic fields of circularly polarized light describe a helix shown in Figure 1.7b. The naming convention (according to optics textbooks) for left-handed and right-handed circularly polarized light follows the same logic as for the other helices. The helix is described by the E-vectors of the circularly polarized light when the light wave is frozen in time (shown in Fig. 1.7b). In other words, looking from the point of the receiver, the electric field vector of right-handed light ascribes an anti-clockwise motion in a fixed plane over time.

In chiral molecules, it may not be obvious to assign which of the mirrored versions (enantiomers) is left- or right-handed. The handedness of molecules was first reported by Biot [27], who shone linear polarized light on liquids/solutions and observed a rotation of the polarization axis. Pasteur realized that the rotation of light is connected to the geometric structure of the molecules [28]. While identical in chemical composition, the two different enantiomers (like shown in Fig. 1.7c) with the atoms arranged in a mirrored way, rotate the

light the opposite way. Chiral molecules are named after the direction they rotate the linear polarization, like the amino acid shown in Figure 1.7c in its dextrorotatory (right-turning, D, sometimes denoted R or +) and levorotatory (left-turning, L, sometimes denoted S or -) form.

Chiral molecules are common in nature and play important roles in biological processes. The medical interest is large, as many drugs have effects and side-effects depending on their handedness. For example, ibuprofen is sold in a racemic mixture, although the dextrorotatory (D) isomer is the more biologically active [29]. The enantio-pure form is marketed as dexibuprofen or ibuprofen express. In other cases, the opposite enantiomer of a drug may be toxic, like (S)-Thalidomide that is produced in the body from (R)-Thalidomide [30]. Here, the active agent was marketed as Softenon/Contergan, with terrible consequences. Many children born to women taking this drug during pregnancy had severe birth defects.

Strikingly, most helical molecules in living beings are right-handed, an unexpected breaking of symmetry known as the homochirality of life [31,32]. Some proposed solutions to this puzzle hinge on deterministic externally induced mechanisms, e.g., due to cosmic rays or the rotation of the earth. Others explain homochirality as the result of probabilistic processes. Then autocatalysis, the catalysis of the same molecule with the same chirality, leads to an amplification [33] of an initially small, random imbalance.

1.4.1 Chirality-Induced Spin Selectivity (CISS)

Chirality-induced spin selectivity (CISS) was first observed in electrons photoemitted from a film of chiral molecules. The CISS effect describes an asymmetry of the spin population, or spin polarization, induced for electrons passing through chiral molecules. The effect is extraordinarily large and lacks a good understanding.

In 1999, Ray et al. [34] shone circularly polarized UV light on layers of stearoyl lysine and measured the photoemission yield. Their data is shown in Figure 1.8a. They reported a large difference in photoemissivity between left- and right-circularly polarized light for the film consisting of five layers of L-stearoyl lysine, which they attributed to a spin-filtering effect in the molecular film. As the spin-population photoemitted from the underlying gold depends on the handedness of the light [35], different transmissivities for each spin would lead to an intensity difference in detected electron flux. For five monolayers, consisting of 99% L-stearoyl lysine and 1% R-stearoyl lysine, they reported the absence of spin-selectivity (Fig. 1.8b), suggesting that spin-selectivity is indeed a collective phenomenon in the layer.

In a later photoemission experiment, Göhler et al. [36] directly measured the spin polarization of the photoelectrons emitted from monolayers of DNA, as shown in Figure 1.8c-e. The degree of spin-polarization P is defined as $P = (I_\mathrm{p} - I_\mathrm{ap})/(I_\mathrm{p} + I_\mathrm{ap})$ with $I_\mathrm{p/ap}$ being the count of electrons with spin parallel/anti-parallel to their direction of travel, respectively. Göhler et al. found a degree of polarization of up to $P = -57\%$ (i.e., preferring spin anti-parallel to the direction of travel, see Fig. 1.8d) depending on the length of the DNA strands. The reported spin polarization of photoemitted electrons depends slightly on the polarization of the light, with $|P|$ increasing from right circularly polarized light (Fig. 1.8c), over linearly polarized light (Fig. 1.8d) to left circularly polarized light (Fig. 1.8e). They attribute this dependence on light

polarization to the asymmetric spin-polarization (due to spin orbit coupling) of the electron population emitted from the underlying gold, which is then filtered by the chiral molecular layer. Independent of the light polarization, the majority of the spins is oriented anti-parallel to the direction of travel. For a compilation of spin polarizations measured in different chiral molecules see [37].

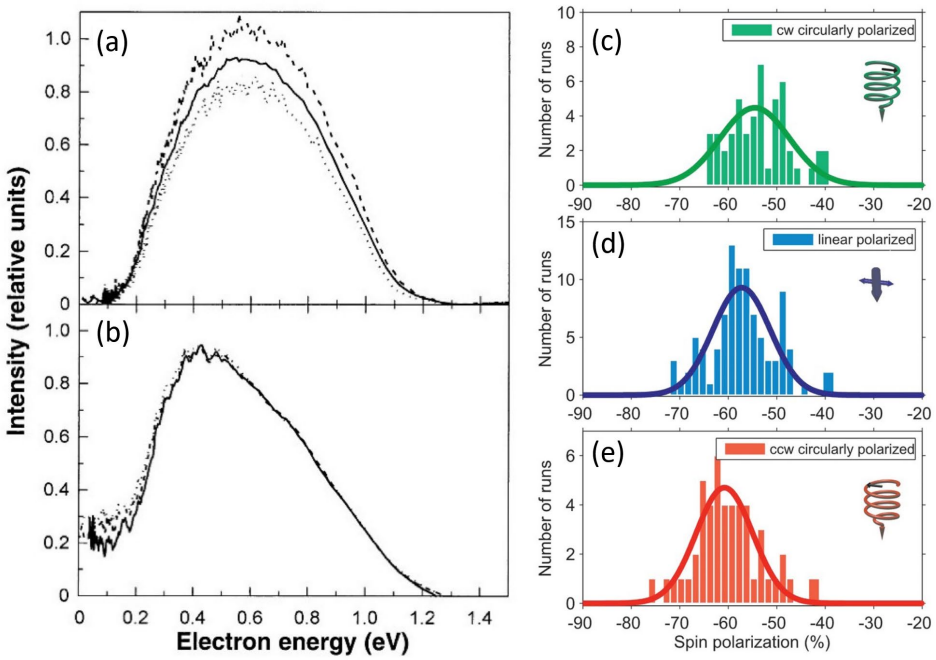

Figure 1.8: Photoemission experiments on chiral molecular layers. Ray et al. [34] measured a difference of photoemission intensity between right-handed circularly polarized light (dashed lines) and left- handed circularly polarized light (dotted lines) in layers of pure L-stearoyl lysine (a), whereas there was no such difference in the non-enantiopure layers (b). Later, Göhler et al. [36] measured the degree of spin polarization (parallel to the electron travel direction) of electrons photoemitted from DNA (c-e). The polarization of the light (indicated in c-e) changes the degree of spin-polarization, but the spin population is still polarized anti-parallel to the direction of travel in all cases. Reprinted from [34] (a,b) and [36] (c-e) with permission from AAAS.

In support of its discovery in photoemission experiments, CISS-related effects have also been reported in scanning tunneling microscopy (STM)/conductive atomic force microscopy (conductive AFM) experiments [38–40], spin-transport devices [41] and catalysis experiments [42–44]. While the scanning probe experiments can measure spin-dependent current-voltage spectra, it is often unclear whether they probe a single chiral molecule or a collective phenomenon of hundreds of molecules. Typically, STM/conductive AFM measurements of current-voltage (IV) curves show a high variance from site to site. This variability is attributed to both the contact of the STM/AFM tip to the molecule and the orientation/environment of the molecule itself. Hence, IV curves in these techniques are measured on hundreds of sites, to check if the average of these spectra shows the asymmetries typical of CISS [38]. Moreover, for all conductance experiments measuring the local

current/voltage, time reversal symmetry forbids a CISS effect at least in linear response, i.e., at low bias [45].

Effects related to CISS have also been shown in catalysis with help of chiral molecules. Chiral molecules (namely L/D-tryptophan, L-A3 and L-A11) attached to Fe_3O_4 nanoparticles were shown to suppress the generation of H_2O_2 byproduct in water splitting [42], in contrast to achiral molecules. The reported efficiency gain in catalysis by chiral molecules may be an explanation for the ubiquity of chiral molecules, and the homochirality, in biological processes.

The CISS effect is also of fundamental scientific interest, as there is no theory fully explaining it yet. The variety of experiments reporting spin-polarization establishes that the CISS effect is present (and large) over a broad range of energies. Transport measurements probe the energies around the Fermi level, chemical reactions mostly depend on the alterations of the highest occupied molecular orbital/lowest unoccupied molecular orbital (HOMO/LUMO), and photoemission experiments probe energies above the vacuum level, thus up to 6 eV higher than the Fermi level. An all-encompassing theory explaining the CISS effect should work over this entire energy range.

The degree of spin polarization found in experiments cannot be quantitatively explained by spin orbit coupling alone because of the low mass of the atoms involved. In a simple model of helically arranged scattering centers, amplification of the spin-orbit terms due to constructive interference of the partial waves was proposed, but its quantitative effect on experiments is unclear [46]. Recent studies attempt to explain the CISS effect as intrinsically related to disorder that diminishes at low temperatures [47]. For a comprehensive review of experimental and theoretical studies and remaining open questions we refer to [48].

While photoemission experiments appear to be the most consistent way to measure CISS, only large-area ($\approx 1\ \mathrm{cm}^2$) averages of photoemission spin selectivity have been reported so far. The scanning probe experiments reported so far, however, show that there is a large site-dependent variability in the spin-polarization [38]. In fact, it is reasonable that the spin-polarization depends on the direct environment of the molecule, e.g. through ordering and (re-)orientation of the surrounding molecules, when we see CISS as a collective phenomenon of the layer, like Ray et al. concluded [34].

Hence, we will set out to use the imaging capabilities of the ESCHER (Electronic, Structural, and Chemical Nanoimaging in Real Time) setup, described in the next chapter, to acquire a two-dimensional map of the polarization-dependent photoelectron intensity. Our method should allow us to spot local differences and hence relate a possible CISS effect to local defects and/or other variations in the molecular layer structure. As we have no means of measuring spin directly in our ESCHER setup, we instead control the handedness of light and image the resulting photoemission intensity. The left/right circular polarization of the light leads to a non-zero spin polarization for the electrons photoemitted from the substrate. According to the studies by Ray et al. and Göhler et al. [36] we should expect an electron intensity difference between right and left circular light on the order of 10% after electrons pass through the molecular layer.

1.5 Outline of this thesis

In this thesis we will study elastic and inelastic interactions of electrons with van der Waals materials as well as the interaction of electron spins with organic molecules. In all cases, the energy of the probing electrons will be higher than the electron vacuum level. The latter energy, which we will generally refer to as the 'zero' energy in this thesis, lies above the Fermi level, the difference between both characteristic energies being the material's work function.

The electron microscopy techniques used throughout this thesis are introduced in **Chapter 2**. Low energy electron microscopy (LEEM) and electron Volt-transmission electron microscopy (eV-TEM) will be utilized to measure the reflection and transmission of electrons in van der Waals materials. Photoemission electron microscopy (PEEM), especially with polarized light, will be used to investigate the CISS effect.

In **Chapter 3** we discuss the transmission and reflection of electrons on few-layer graphene. The elastic scattering processes, leading to resonances in the spectra discussed above, can be explained in a toy model based on interference [22]. However, there has been a debate on how to extract inelastic and elastic MFPs correctly from the low-energy reflection and transmission [49]. We extend the toy model to include inelastic contributions, and thus reconcile the elastic and inelastic view, and directly extract inelastic and elastic MFPs from that model.

The transmission and reflection from a heterostructure of hBN stacked on graphene is investigated in **Chapter 4**. The heterostructure breaks the up-down symmetry with respect to the direction of travel of the electrons. Thus, the effect of symmetry breaking on electron transmission and reflection is investigated and compared to *ab-initio* calculations and a modified toy model.

In **Chapter 5** we investigate few-layer molybdenum disulfide (MoS_2), which has a more complicated out-of-plane structure than graphene (see Fig. 1.1). Connected to that geometric difference, we find distinct high-electron-transmissivity windows connected to the band structure. We compare the mean free paths obtained by our technique with those reported in previous photoemission studies.

Chapter 6 is dedicated to the first steps in imaging polarization-dependent photoemission from chiral molecular layers using PEEM. We first report on photoemission measurements of plasmonic gold structures with linear polarized light. Then, we consider a film of chiral molecules (R-2,2′-bis(diphenylphosphino)-1,1′-binaphthyl, R-BINAP) for which we measure its photoemissivity upon illumination with left- and right-elliptically polarized light.

References

[1] A. Falin, Q. Cai, E.J.G. Santos, D. Scullion, D. Qian, R. Zhang, Z. Yang, S. Huang, K. Watanabe, T. Taniguchi, M.R. Barnett, Y. Chen, R.S. Ruoff, L.H. Li, Mechanical properties of atomically thin boron nitride and the role of interlayer interactions, Nat. Commun. 8 (2017) 1–9. https://doi.org/10.1038/ncomms15815.

[2] Y. Yang, Z. Song, G. Lu, Q. Zhang, B. Zhang, B. Ni, C. Wang, X. Li, L. Gu, X. Xie, H. Gao, J. Lou, Intrinsic toughening and stable crack propagation in hexagonal boron nitride, Nature 594 (2021) 57–61. https://doi.org/10.1038/s41586-021-03488-1.

[3] K. Cao, S. Feng, Y. Han, L. Gao, T. Hue Ly, Z. Xu, Y. Lu, Elastic straining of free-standing monolayer graphene, Nat. Commun. 11 (2020) 284. https://doi.org/10.1038/s41467-019-14130-0.

[4] P.R. Wallace, The Band Theory of Graphite, Phys. Rev. 71 (1947) 622–634. https://doi.org/10.1103/PhysRev.71.622.

[5] H. Min, B. Sahu, S.K. Banerjee, A.H. MacDonald, Ab initio theory of gate induced gaps in graphene bilayers, Phys. Rev. B - Condens. Matter Mater. Phys. 75 (2007) 1–7. https://doi.org/10.1103/PhysRevB.75.155115.

[6] Y. Cao, V. Fatemi, S. Fang, K. Watanabe, T. Taniguchi, E. Kaxiras, P. Jarillo-Herrero, Unconventional superconductivity in magic-angle graphene superlattices, Nature 556 (2018) 43–50. https://doi.org/10.1038/nature26160.

[7] S. Lisi, X. Lu, T. Benschop, T.A. de Jong, P. Stepanov, J.R. Duran, F. Margot, I. Cucchi, E. Cappelli, A. Hunter, A. Tamai, V. Kandyba, A. Giampietri, A. Barinov, J. Jobst, V. Stalman, M. Leeuwenhoek, K. Watanabe, T. Taniguchi, L. Rademaker, S.J. van der Molen, M.P. Allan, D.K. Efetov, F. Baumberger, Observation of flat bands in twisted bilayer graphene, Nat. Phys. 17 (2021) 189–193. https://doi.org/10.1038/s41567-020-01041-x.

[8] E. Suárez Morell, J.D. Correa, P. Vargas, M. Pacheco, Z. Barticevic, Flat bands in slightly twisted bilayer graphene: Tight-binding calculations, Phys. Rev. B 82 (2010) 121407. https://doi.org/10.1103/PhysRevB.82.121407.

[9] K.S. Novoselov, A.K. Geim, S. V. Morozov, D. Jiang, Y. Zhang, S. V. Dubonos, I.V. Grigorieva, A.A. Firsov, Electric Field Effect in Atomically Thin Carbon Films, Science (80-.). 306 (2004) 666–669. https://doi.org/10.1126/science.1102896.

[10] J. Klein, M. Lorke, M. Florian, F. Sigger, L. Sigl, S. Rey, J. Wierzbowski, J. Cerne, K. Müller, E. Mitterreiter, P. Zimmermann, T. Taniguchi, K. Watanabe, U. Wurstbauer, M. Kaniber, M. Knap, R. Schmidt, J.J. Finley, A.W. Holleitner, Site-selectively generated photon emitters in monolayer MoS2 via local helium ion irradiation, Nat. Commun. 10 (2019) 1–8. https://doi.org/10.1038/s41467-019-10632-z.

[11] D. Geelen, A. Thete, O. Schaff, A. Kaiser, S.J. van der Molen, R. Tromp, eV-TEM: Transmission electron microscopy in a low energy cathode lens instrument, Ultramicroscopy 159 (2015) 482–487. https://doi.org/10.1016/j.ultramic.2015.06.014.

[12] H. Hibino, S. Wang, C.M. Orofeo, H. Kageshima, Growth and low-energy electron microscopy characterizations of graphene and hexagonal boron nitride, Prog. Cryst. Growth Charact. Mater. 62 (2016) 155–176. https://doi.org/10.1016/j.pcrysgrow.2016.04.008.

[13] H. Hibino, H. Kageshima, F. Maeda, M. Nagase, Y. Kobayashi, Y. Kobayashi, H. Yamaguchi, Thickness Determination of Graphene Layers Formed on SiC Using Low-Energy Electron Microscopy, E-Journal Surf. Sci. Nanotechnol. 6 (2008) 107–110. https://doi.org/10.1380/ejssnt.2008.107.

[14] J. Jobst, J. Kautz, D. Geelen, R.M. Tromp, S.J. van der Molen, Nanoscale measurements of unoccupied band dispersion in few-layer graphene, Nat. Commun. 6 (2015) 8926. https://doi.org/10.1038/ncomms9926.

[15] D.J. Griffiths, Time-Independent Schrödinger Equation, in: Introd. to Quantum Mech. ISBN 0131911759, 2nd ed., 2004.

[16] K. Konishi, G. Paffuti, The Schrödinger equation, in: Quantum Mech., Oxford University PressOxford, 2009: pp. 49–88. https://doi.org/10.1093/oso/9780199560264.003.0003.

[17] B. Stec, C. Jędrzejek, Resonance scattering by a double square-well potential, Eur. J. Phys. 11 (1990) 75–81. https://doi.org/10.1088/0143-0807/11/2/002.

[18] V.U. Nazarov, E.E. Krasovskii, V.M. Silkin, Scattering resonances in two-dimensional crystals with application to graphene, Phys. Rev. B - Condens. Matter Mater. Phys. 87 (2013) 1–5. https://doi.org/10.1103/PhysRevB.87.041405.

[19] K.D. Pham, H. V. Phuc, N.N. Hieu, B.D. Hoi, C. V. Nguyen, Electronic properties of GaSe/MoS2 and GaS/MoSe2 heterojunctions from first principles calculations, AIP Adv. 8 (2018). https://doi.org/10.1063/1.5033348.

[20] M.P. Seah, W.A. Dench, Quantitative electron spectroscopy of surfaces: A standard data base for electron inelastic mean free paths in solids, Surf. Interface Anal. 1 (1979) 2–11. https://doi.org/10.1002/sia.740010103.

[21] W.S.M. Werner, Questioning a Universal Law for Electron Attenuation, Physics (College. Park. Md). 12 (2019) 93. https://doi.org/10.1103/Physics.12.93.

[22] D. Geelen, J. Jobst, E.E. Krasovskii, S.J. van der Molen, R.M. Tromp, Nonuniversal Transverse Electron Mean Free Path through Few-layer Graphene, Phys. Rev. Lett. 123 (2019) 086802. https://doi.org/10.1103/PhysRevLett.123.086802.

[23] P.S. Neu, D. Geelen, A. Thete, R.M. Tromp, S.J. van der Molen, Complementary LEEM and eV-TEM for imaging and spectroscopy, Ultramicroscopy 222 (2021) 113199. https://doi.org/10.1016/j.ultramic.2020.113199.

[24] P.S. Neu, M. Šiškins, E.E. Krasovskii, R.M. Tromp, S.J. van der Molen, Electron transmission and mean free path in molybdenum disulfide at electron-volt energies, Phys. Rev. B 107 (2023) 075427. https://doi.org/10.1103/PhysRevB.107.075427.

[25] Wikipedia: Circular polarization, (n.d.). https://en.wikipedia.org/wiki/Circular_polarization (accessed January 5, 2024).

[26] M. Inaki, J. Liu, K. Matsuno, Cell chirality: Its origin and roles in left-right asymmetric development, Philos. Trans. R. Soc. B Biol. Sci. 371 (2016). https://doi.org/10.1098/rstb.2015.0403.

[27] J.-B. Biot, Phénomènes de polarisation successive, observés dans des fluides homogènes, Bull. Soc. Philomath 190 (1815) 1815.

[28] H.D. Flack, Louis Pasteur's discovery of molecular chirality and spontaneous resolution in 1848, together with a complete review of his crystallographic and chemical work, Acta Crystallogr. Sect. A Found. Crystallogr. 65 (2009) 371–389. https://doi.org/10.1107/S0108767309024088.

[29] D. Lowe, Right Hand, Left Hand, Either Hand, (n.d.). https://www.science.org/content/blog-post/right-hand-left-hand-either-hand (accessed January 4, 2024).

[30] T. Eriksson, S. Bjöurkman, B. Roth, Å. Fyge, P. Höuglund, Stereospecific determination, chiral inversion in vitro and pharmacokinetics in humans of the enantiomers of thalidomide, Chirality 7 (1995) 44–52. https://doi.org/10.1002/chir.530070109.

[31] J.L. Bada, Origins of homochirality, Nature 374 (1995) 594–595. https://doi.org/10.1038/374594a0.

[32] S.F. Ozturk, D.D. Sasselov, J.D. Sutherland, The central dogma of biological homochirality: How does chiral information propagate in a prebiotic network?, J. Chem. Phys. 159 (2023). https://doi.org/10.1063/5.0156527.

[33] F.C. Frank, On spontaneous asymmetric synthesis, Biochim. Biophys. Acta 11 (1953) 459–463. https://doi.org/10.1016/0006-3002(53)90082-1.

[34] K. Ray, S.P. Ananthavel, D.H. Waldeck, R. Naaman, Asymmetric scattering of polarized electrons by organized organic films of chiral molecules, Science (80-.). 283 (1999) 814–816. https://doi.org/10.1126/science.283.5403.814.

[35] F. Meier, D. Pescia, Band-Structure Investigation of Gold by Spin-Polarized Photoemission, Phys. Rev. Lett. 47 (1981) 374–377. https://doi.org/10.1103/PhysRevLett.47.374.

[36] B. Göhler, V. Hamelbeck, T.Z. Markus, M. Kettner, G.F. Hanne, Z. Vager, R. Naaman, H. Zacharias, Spin selectivity in electron transmission through self-assembled monolayers of double-stranded DNA - Supplementary Information, Science (80-.). 331 (2011) 894–897. https://doi.org/10.1126/science.1199339.

[37] C. Clever, E. Wierzbinski, B.P. Bloom, Y. Lu, H.M. Grimm, S.R. Rao, W.S. Horne, D.H. Waldeck, Benchmarking Chiral Induced Spin Selectivity Measurements - Towards Meaningful Comparisons of Chiral Biomolecule Spin Polarizations, Isr. J. Chem. 62 (2022) 1–14. https://doi.org/10.1002/ijch.202200045.

[38] Z. Xie, T.Z. Markus, S.R. Cohen, Z. Vager, R. Gutierrez, R. Naaman, Spin specific electron conduction through DNA oligomers, Nano Lett. 11 (2011) 4652–4655. https://doi.org/10.1021/nl2021637.

[39] M. Suda, Y. Thathong, V. Promarak, H. Kojima, M. Nakamura, T. Shiraogawa, M. Ehara, H.M. Yamamoto, Light-driven molecular switch for reconfigurable spin filters, Nat. Commun. 10 (2019) 2455. https://doi.org/10.1038/s41467-019-10423-6.

[40] A.K. Mondal, M.D. Preuss, M.L. Ślęczkowski, T.K. Das, G. Vantomme, E.W. Meijer, R. Naaman, Spin Filtering in Supramolecular Polymers Assembled from Achiral Monomers Mediated by Chiral Solvents, J. Am. Chem. Soc. 143 (2021) 7189–7195. https://doi.org/10.1021/jacs.1c02983.

[41] T. Liu, X. Wang, H. Wang, G. Shi, F. Gao, H. Feng, H. Deng, L. Hu, E. Lochner, P. Schlottmann, S. Von Molnár, Y. Li, J. Zhao, P. Xiong, Linear and nonlinear two-terminal spin-valve effect from chirality-induced spin selectivity, ACS Nano 14 (2020) 15983–15991. https://doi.org/10.1021/acsnano.0c07438.

[42] W. Zhang, K. Banerjee-Ghosh, F. Tassinari, R. Naaman, Enhanced Electrochemical Water Splitting with Chiral Molecule-Coated Fe3O4 Nanoparticles, ACS Energy Lett. 3 (2018) 2308–2313. https://doi.org/10.1021/acsenergylett.8b01454.

[43] P.K. Bhartiya, M. Srivastava, D. Mishra, Chiral-induced enhanced electrocatalytic behaviour of cysteine coated bifunctional Au–Ni bilayer thin film device for water splitting application, Int. J. Hydrogen Energy 47 (2022) 42160–42170. https://doi.org/10.1016/j.ijhydene.2021.08.219.

[44] K.B. Ghosh, W. Zhang, F. Tassinari, Y. Mastai, O. Lidor-Shalev, R. Naaman, P. Möllers, D. Nürenberg, H. Zacharias, J. Wei, E. Wierzbinski, D.H. Waldeck, Controlling Chemical Selectivity in Electrocatalysis with Chiral CuO-Coated Electrodes, J. Phys. Chem. C 123 (2019) 3024–3031. https://doi.org/10.1021/acs.jpcc.8b12027.

[45] X. Yang, C.H. van der Wal, B.J. van Wees, Detecting Chirality in Two-Terminal Electronic Nanodevices, Nano Lett. 20 (2020) 6148–6154. https://doi.org/10.1021/acs.nanolett.0c02417.

[46] J.M. van Ruitenbeek, R. Korytár, F. Evers, Chirality-controlled spin scattering through quantum interference, J. Chem. Phys. 159 (2023). https://doi.org/10.1063/5.0156316.

[47] T.K. Das, F. Tassinari, R. Naaman, J. Fransson, Temperature-Dependent Chiral-Induced Spin Selectivity Effect: Experiments and Theory, J. Phys. Chem. C 126 (2022) 3257–3264. https://doi.org/10.1021/acs.jpcc.1c10550.

[48] F. Evers, A. Aharony, N. Bar-Gill, O. Entin-Wohlman, P. Hedegård, O. Hod, P. Jelinek, G. Kamieniarz, M. Lemeshko, K. Michaeli, V. Mujica, R. Naaman, Y. Paltiel, S. Refaely-Abramson, O. Tal, J. Thijssen, M. Thoss, J.M. van Ruitenbeek, L. Venkataraman, D.H. Waldeck, B. Yan, L. Kronik, Theory of Chirality Induced Spin Selectivity: Progress and Challenges, Adv. Mater. 34 (2022) 1–11. https://doi.org/10.1002/adma.202106629.

[49] L.H. Yang, B. Da, H. Yoshikawa, S. Tanuma, J. Hu, J.W. Liu, D.M. Tang, Z.J. Ding, Low-energy electron inelastic mean free path and elastic mean free path of graphene, Appl. Phys. Lett. 118 (2021) 053104. https://doi.org/10.1063/5.0029133.